

A High Fraction of Heavily X-ray Obscured Active Galactic Nuclei

CHRISTOPHER M. CARROLL ^{1,2} TONIMA T. ANANNA ² RYAN C. HICKOX ² ALBERTO MASINI ^{3,4} ROBERTO J. ASSEF ⁵
DANIEL STERN ⁶ CHIEN-TING J. CHEN ⁷ AND LAURANNE LANZ ⁸

¹*Department of Physics and Astronomy, Washington State University, 1245 Webster Hall, Pullman, WA 99164, USA*

²*Department of Physics and Astronomy, Dartmouth College, 6127 Wilder Laboratory, Hanover, NH 03755, USA*

³*SISSA, Via Bonomea 265, 34151 Trieste, Italy*

⁴*INAF – Osservatorio di Astrofisica e Scienza dello Spazio di Bologna, via Gobetti 93/3, I-40129 Bologna, Italy*

⁵*Núcleo de Astronomía de la Facultad de Ingeniería y Ciencias, Universidad Diego Portales, Av. Ejército Libertador 441, Santiago, Chile*

⁶*Jet Propulsion Laboratory, California Institute of Technology, 4800 Oak Grove Drive, Mail Stop 169-221, Pasadena, CA 91109, USA*

⁷*Astrophysics Office, NASA Marshall Space Flight Center, ZP12, Huntsville, AL 35812, USA*

⁸*Department of Physics, The College of New Jersey, 2000 Pennington Road, Ewing, NJ 08628, USA*

(Received September 26, 2021; Revised May 6, 2022; March 3, 2023; Accepted March 9, 2023)

Submitted to ApJ

ABSTRACT

We present new estimates on the fraction of heavily X-ray obscured, Compton-thick (CT) active galactic nuclei (AGNs) out to a redshift of $z \leq 0.8$. From a sample of 540 AGNs selected by mid-IR (MIR) properties in observed X-ray survey fields, we forward model the observed-to-intrinsic X-ray luminosity ratio (R_{L_X}) with a Markov chain Monte Carlo (MCMC) simulation to estimate the total fraction of CT AGNs (f_{CT}), many of which are missed in typical X-ray observations. We create model N_H distributions and convert these to R_{L_X} using a set of X-ray spectral models. We probe the posterior distribution of our models to infer the population of X-ray non-detected sources. From our simulation we estimate a CT fraction of $f_{CT} = 0.555^{+0.037}_{-0.032}$. We perform an X-ray stacking analysis for sources in Chandra X-ray Observatory fields and find that the expected soft (0.5–2 keV) and hard (2–7 keV) observed fluxes drawn from our model to be within 0.48 and 0.12 dex of our stacked fluxes, respectively. Our results suggests at least 50% of all MIR-selected AGNs, possibly more, are Compton-thick ($N_H \gtrsim 10^{24} \text{ cm}^{-2}$), which is in excellent agreement with other recent work using independent methods. This work indicates that the total number of AGNs is higher than can be identified using X-ray observations alone, highlighting the importance of a multiwavelength approach. A high f_{CT} also has implications for black hole (BH) accretion physics and supports models of BH and galaxy co-evolution that include periods of heavy obscuration.

Keywords: Active galactic nuclei (16) — Active galaxies (17) — Luminous infrared galaxies (946) — Surveys (1671) — X-ray surveys (1824) — X-ray active galactic nuclei (2035)

1. INTRODUCTION

Supermassive black holes (SMBHs) are found ubiquitously at the centers of massive galaxies, growing via intermittent accretion of interstellar material and occasional SMBH mergers. During intense periods of gas accretion, these active galactic nuclei (AGNs) are extremely luminous, radiating across the electromagnetic spectrum. Since the seminal discovery that obscuring dust is responsible for the observed difference between broad-line and narrow-line AGNs (Antonucci & Miller 1985; see Ricci et al. 2017; Ananna et al. 2022a,b for more recent models of unification), major efforts have been undertaken to characterize the nature and extent of the obscuring material, with attempts to determine its composition (e.g., Davies et al. 2015; García-Burillo et al. 2016) and physical scale (e.g., Hönig et al. 2012;

Tristram et al. 2014; Chen et al. 2015; López-Gonzaga et al. 2016; Panagiotou & Walter 2019). Obscuration across electromagnetic regimes is also thought to originate from different sources, namely nuclear gas producing absorption at X-ray energies and circumnuclear dust grains causing extinction of UV and optical emission (see Hickox & Alexander 2018).

Infrared surveys have provided evidence that more than half of the AGN population exhibit signatures of obscuration (Lacy et al. 2013). Optical–near-IR (NIR) colors have proven reliable in selecting obscured sources in large AGN samples (e.g., Hickox et al. 2007; LaMassa et al. 2016) but lack the power to accurately estimate levels of obscuration, particularly in heavily obscured sources where the host galaxy dominates at optical and NIR wavelengths. Mid-IR (MIR) tech-

niques have further improved our ability to probe heavily obscured AGN that are missed by optical surveys (e.g., Stern et al. 2005, 2012; Mateos et al. 2013; Assef et al. 2015), as MIR observations probe emission from dust and are relatively unaffected by dust obscuration.

While MIR observations have contributed reliable techniques for identifying obscured AGNs, X-ray spectroscopic observations have become the dominant method of probing nuclear obscuring gas content (see Hickox & Alexander 2018), the bulk of which need not necessarily trace the distribution of dust. Though the X-ray regime has become the favored method for measuring obscuring column densities (N_{H}), recent work has shown that hard X-ray energies ($\geq 2\text{--}10$ keV) can remain undetected for heavily obscured AGN in typical observations (e.g., Lansbury et al. 2015; Yan et al. 2019; Lambrides et al. 2020). This provides a particular challenge for Compton-thick (CT) densities (i.e., $N_{\text{H}} \geq 1.5 \times 10^{24} \text{ cm}^{-2}$), where scattering optical depths reach order unity (e.g., Lansbury et al. 2015). As deep, hard X-ray observations are required to positively identify and constrain the density of obscuring material surrounding CT AGNs (e.g., Traina et al. 2021), large-scale searches have been limited to smaller fields. To date there has been no reliable direct measure of the complete fraction of CT AGN (f_{CT}), marking a major uncertainty in the total number of accreting black holes (BHs) in the universe. New techniques are therefore required to accurately measure the line-of-sight gas densities for the most heavily obscured AGNs, and enable a complete view of the population (e.g., Pfeifle et al. 2021).

One compelling approach involves utilizing the empirical relationship between the X-ray and MIR luminosities (L_{X} and L_{MIR} respectively) of AGNs (i.e., Fiore et al. 2009; Stern 2015; Chen et al. 2017). The combination of X-ray and MIR luminosities has been shown to provide a reliable method for identifying extremely obscured AGNs ($N_{\text{H}} > 10^{24} \text{ cm}^{-2}$) in large samples (e.g., Carroll et al. 2021, hereafter C21). The $L_{\text{X}}\text{--}L_{\text{MIR}}$ relation provides a method of inferring the intrinsic X-ray luminosity of an AGN through its MIR luminosity ($L_{\text{X}}(L_{\text{MIR}})$), which is reasonably straightforward to estimate given the quality and depth of all-sky IR data. The ratio of the observed-to-intrinsic X-ray luminosity ($R_{L_{\text{X}}}$) then provides insight into the amount of obscuring material present in a given source and can be calculated directly from observables. X-ray spectral models provide the final component, allowing us to understand the effects of increasing N_{H} on observed X-ray fluxes and ultimately $R_{L_{\text{X}}}$.

Moreover, C21 showed that the same technique can be used to estimate lower limits on N_{H} for sources that are not detected in X-ray observations, substituting X-ray flux limits in lieu of direct detections. However, the $R_{L_{\text{X}}}$ distribution for X-ray detected and non-detected sources differs drastically and cannot be directly compared, as $R_{L_{\text{X}}}$ for non-detected sources are upper limits. As such, N_{H} can only be estimated with any given accuracy for X-ray detected sources using this methodology. Therefore, a new statistical method is required

to include the X-ray non-detected sources in our estimates of the distribution of N_{H} .

Previous studies have estimated the space density of AGNs—including CT sources—predominantly through modeling of the X-ray luminosity function (XLF; i.e., Ueda et al. 2014; Buchner et al. 2015; Aird et al. 2015; Fotopoulou et al. 2016; Ananna et al. 2019), which describes the number density of AGNs as a function of X-ray luminosity and redshift. This approach is dependent on large samples of X-ray selected AGNs in soft and hard energies. Additionally, this method is generally reliant on assuming an absorption function to account for obscuration and/or modeling of obscured and unobscured sources separately. Multiple observational constraints may be used in the generation of the XLF through synthesis models, including X-ray number counts, spectral shape of the integrated cosmic X-ray background (CXB), and the observed fraction of CT AGNs. The latest synthesis models produce an XLF out to $z = 1$ that accounts for all observational constraints (Ananna et al. 2019, hereafter A19), predicting a CT fraction of 0.50 ± 0.09 for low- to moderate-luminosity AGNs ($\log L_{\text{X}}/\text{erg s}^{-1} < 43.6$), and as high as 0.56 ± 0.07 at higher luminosities ($\log L_{\text{X}}/\text{erg s}^{-1} > 43.6$)—much higher than previous studies.

In this work, we aim to make a direct measurement of f_{CT} and determine the underlying N_{H} distribution of heavily obscured sources ($N_{\text{H}} \geq 10^{24} \text{ cm}^{-2}$). Our approach relies on multiwavelength archival data to account for AGNs which are either undetected or poorly detected in the X-rays. We use a novel multiwavelength, non-parametric approach to forward model the N_{H} distribution by simulating the observed $R_{L_{\text{X}}}$ distribution in a complete sample of AGNs.

This paper is organized as follows: Section 2 details our photometric sample and matching X-ray fields; Section 3 describes our modeling procedure; Section 4 details our analysis and results of our modeling; Section 5 summarizes our results and future work. Throughout the paper, we assume a Λ CDM cosmology with parameters $H_0 = 70 \text{ km s}^{-1} \text{ Mpc}^{-1}$, $\Omega_{\text{m}} = 0.3$, and $\Omega_{\Lambda} = 0.7$ (Spergel et al. 2007).

2. DATA

The sample adopted in this paper builds on previous work by C21, having identified heavily obscured AGNs from multiwavelength archival data. The details of their data selection and modeling are fully described therein and briefly summarized here.

Our sample consists of 540 AGNs selected on the basis of MIR colors (Assef et al. 2018) from the Wide-field Infrared Survey Explorer (WISE; Wright et al. 2010) and matched to Sloan Digital Sky Survey (SDSS; York et al. 2000) optical counterparts. Each source in our sample also lies within fields observed by the Chandra (Evans et al. 2020), XMM-Newton (Rosen et al. 2016), and/or NuSTAR (Civano et al. 2015; Lansbury et al. 2017; Masini et al. 2018) X-ray observatories. Although the 540 sources in our final sample all lie within observed X-ray fields, only 40% have X-ray detections, with the remaining 60% lacking X-ray counter-

parts. This working sample was drawn from a larger parent dataset of over three million sources with redshift measurements (photometric and spectroscopic), each with matching SDSS–WISE photometry.

Optical photometry for our sample was obtained from a combination of SDSS Data Release 14 (Abolfathi et al. 2018) and XDQSOz (DiPompeo et al. 2015). In this work, we chose to replace all MIR photometry from the WISE AllWISE Source Catalog with unWISE (Lang 2014). The unWISE Catalog produced WISE forced photometry at known SDSS source positions, ensuring reliable source association across catalogs. Use of the unWISE Catalog increases the depth of WISE observations at wavelengths crucial to disentangling absorbed and non-absorbed systems, all while maintaining the highest possible signal-to-noise ratio (S/N). Additional photometry was added in UV and NIR bands where available from the Galaxy Evolution Explorer (GALEX; Martin et al. 2005), the UKIRT Infrared Deep Sky Survey (UKIDSS; Lawrence et al. 2007), and the Two Micron All Sky Survey (2MASS; Skrutskie et al. 2006) (see C21 for additional details).

To ensure the accuracy of our modeling and minimize systematics, we imposed several quality selection criteria to our data. First, we required all available photometry to have a minimum $S/N \geq 3.0$. We required a minimum of seven photometric bands per source for adequate coverage to model spectral energy distributions (SEDs), with the additional requirement of detections in all four WISE bands to accurately constrain AGN contribution to the MIR. SDSS photometry was only considered where the PhotoObjAll column `clean = 1`, ensuring reliable photometry. Though our data was primarily WISE selected, all sources are detected in *gri*. Finally, we applied an angular bright stars mask to remove regions of the sky with possible IR contamination (DiPompeo et al. 2014). We chose to limit sources to redshifts $z \leq 0.8$ and only used SDSS photometric redshifts where the Photoz column `photoErrorClass` was $-1, 1, 2, \text{ or } 3$, corresponding to an average root-mean-square error between $0.066 \leq \text{RMSE} \leq 0.074$. Our final sample consists of sources having 64% photometric and 36% spectroscopic redshifts.

Broadband SEDs were modeled using a combination of galaxy and AGN templates (Assef et al. 2010; Kirkpatrick et al. 2015). From our SED modeling, sources were only considered if they passed a minimum reduced chi-square cut ($\chi^2_{\text{red}} \leq 20.0$) to reject poor fits. We also required sources to derive a high fraction of their total MIR SED emission from AGN contribution ($f_{\text{AGN}} \geq 0.7$ at $15\mu\text{m}$), and further limited our final sample to IR-luminous sources ($L_{\text{MIR}} > 10^{42} \text{ erg s}^{-1}$).

All sources in our final sample contain MIR $6\mu\text{m}$ AGN luminosities (L_{MIR}) drawn directly from our SED modeling. Each object lies within an X-ray observed field and includes 3σ upper-limit X-ray luminosities ($L_{\text{X-lim}}$) for both X-ray detected and non-detected sources, drawn from the respective flux limits of each instrument (see Figure 3 of C21). Observed 2–10 keV X-ray luminosities (L_{X}) were calculated for

the X-ray detected sources in our sample. The observed $L_{\text{X}}-L_{\text{MIR}}$ relation of Chen et al. (2017) was used to estimate intrinsic X-ray luminosities ($L_{\text{X}}(L_{\text{MIR}})$) for all sources, corresponding to their derived MIR AGN luminosities. A breakdown of the sample properties described in this section are shown in Figure 1 and are separated for comparison into X-ray detected and non-detected sources. Lastly, we defined the ratio of observed-to-intrinsic X-ray luminosity as

$$R_{L_{\text{X}}} = \begin{cases} \frac{L_{\text{X}}}{L_{\text{X}}(L_{\text{MIR}})} & \text{for X-ray detected,} \\ \frac{L_{\text{X-lim}}}{L_{\text{X}}(L_{\text{MIR}})} & \text{for X-ray non-detected,} \end{cases} \quad (1)$$

which is used as a proxy for nuclear obscuration.

3. MODELING

3.1. X-Ray Spectral Models

We used a set of X-ray spectral models to estimate the impact of nuclear obscuration on observed AGN X-ray flux. Our spectral models were constructed using the X-ray spectral fitting package XSPEC (Arnaud 1996) with the following syntax:

$$\begin{aligned} & \text{CONSTANT} \times \text{CUTOFFPL} \\ & \quad + \text{ZPHABS} \times \text{CABS} \times \text{PEXMON} \\ & \quad \quad \quad + \text{BORUS02}. \end{aligned}$$

Each of our models follow a similar prescription, being the sum of transmitted, reflected, and scattered components to account for the diversity of AGN X-ray spectra (e.g., Buchner et al. 2014; Ananna et al. 2020).

We began with an initial spectral model CUTOFFPL, consisting of a 300 keV high-energy cutoff power law to represent the intrinsic continuum of UV–optical photons upscattered to X-ray energies through Comptonization by the AGN corona. To account for Thomson scattering of the X-ray continuum by photoionized, circumnuclear material, we assumed the variable scattering fraction of Gupta et al. (2021, hereafter, G21), applied as a multiplicative constant to the cutoff power law. G21 observe that the scattering fraction (f_{scatt}) decreases with increasing N_{H} and shows no dependency on X-ray luminosity or BH mass. To encapsulate any other potential factors due to AGN diversity in our sample, we chose to incorporate the G21 uncertainties on scattering fraction (σ_{scatt}) as a parameter in our model. Though we technically employ the uncertainties on scattering fraction ($f_{\text{scatt}} + \sigma_{\text{scatt}}$) in our models, to avoid unnecessary confusion we refer to this parameter as f_{scatt} except where explicitly necessary.

Next, we considered Compton reflection of X-ray photons by the accretion disk. A fraction of the high-energy continuum photons in proximity to the colder material of the accretion disk are thought to be captured and reprocessed, contributing to an X-ray spectral feature around 30 keV known as the Compton reflection ‘‘hump.’’ For our models we chose

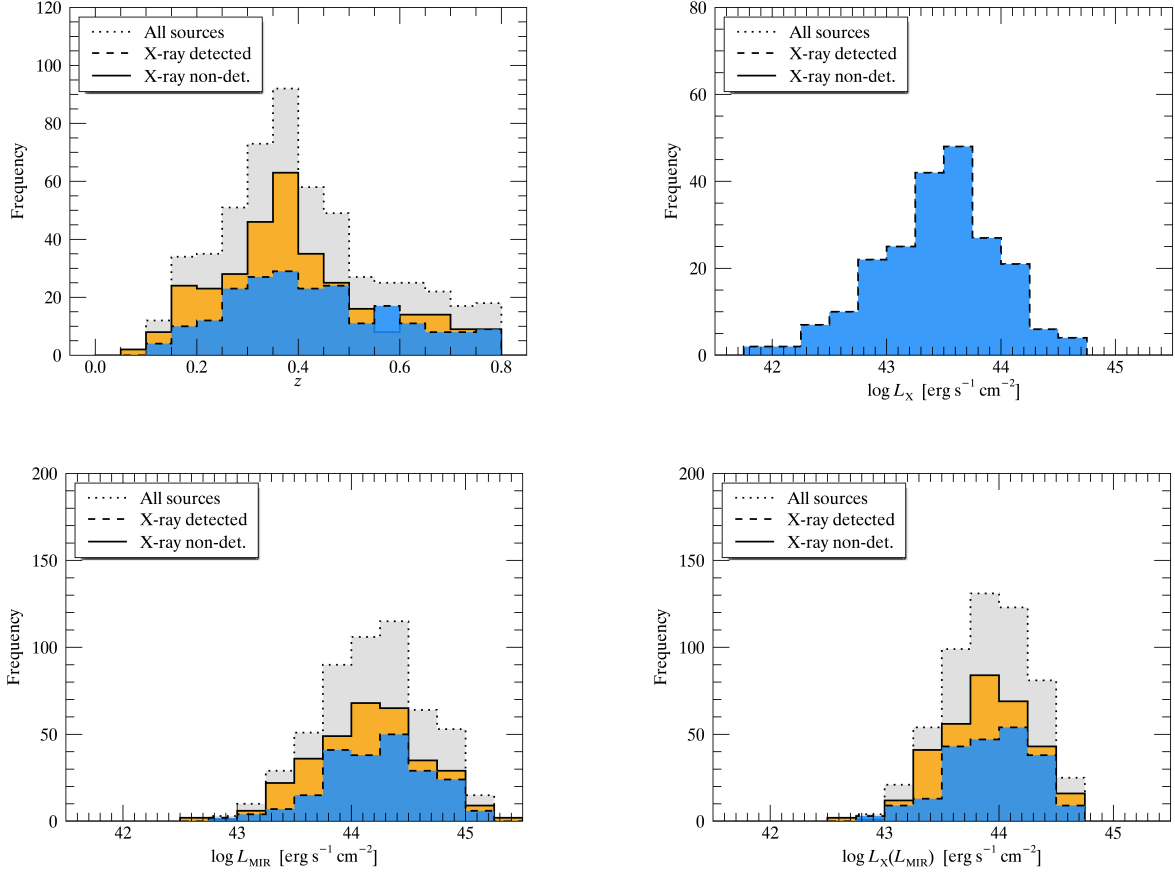


Figure 1. Distribution of sample properties: redshift (z ; top left); observed 2–10 keV X-ray luminosity (L_X ; top right); MIR AGN $6\ \mu\text{m}$ luminosity (L_{MIR} ; bottom left); intrinsic 2–10 keV X-ray luminosity estimates ($L_X(L_{\text{MIR}})$; bottom right). In each panel, the distributions are demarcated as X-ray detected (dashed blue) and X-ray non-detected (solid orange) sources, along with the comprehensive distribution (dotted gray).

to add the PEXMON spectral component, which assumes a simplistic, slab-like geometry of optically thick, cold material. The strength, or scaling factor for reflection (R), was then used as an additional parameter in our model. We then multiplied the reflected component by ZPHABS and CABS to account for attenuation by photoelectric absorption and Compton scattering, respectively.

Finally, we handled attenuation of emission by a more distant, circumnuclear distribution of gas and dust, colloquially referred to as the obscuring torus. For this, we chose to adopt the radiative transfer code of Baloković et al. (2018), specifically BORUS02, representing the AGN torus as a uniform density sphere with polar cutouts and a cutoff power-law intrinsic continuum. As the majority of the attenuation in obscured systems is thought to be caused by nuclear material within the gravitational influence of the central SMBH, the high upper limit of the torus column density parameter of BORUS02 allows us to estimate the effects of extremely high levels of obscuration. The BORUS02 model also accounts for Compton reflection by the torus, further contributing to the Compton hump described above.

Starting at $z = 0$, we increased the line-of-sight column density from $10^{21}\ \text{cm}^{-2}$ to $10^{25}\ \text{cm}^{-2}$ and calculated the change in the observed-to-intrinsic 2–10 keV flux ratio as a function of N_{H} . For this calculation, we adopted the flux at $N_{\text{H}} = 10^{21}\ \text{cm}^{-2}$ as the intrinsic, unobscured X-ray flux. The simulated change in the X-ray spectral model flux ratio provides us with a conversion between N_{H} and R_{L_X} , which we adopted for the body of our work. Though BORUS02 obscuration can be set at higher values, the distinction between sources with column densities higher than the CT limit are not well constrained, thus we chose $N_{\text{H}} = 10^{25}\ \text{cm}^{-2}$ as an upper limit in our models.

We then investigated the effects of different model parameters on R_{L_X} , including scattering fraction f_{scatt} , reflection strength R , photon index (Γ), and torus opening angle (θ_{OA}). Following the prescription above, we constructed spectral models for each set of parameters $\{f_{\text{scatt}}, R, \Gamma, \theta_{\text{OA}}\}$. To account for the extremely low scattering fraction seen in some heavily obscured systems (e.g., Noguchi et al. 2010), we allowed the scattering fraction to vary uniformly between $-2.0 \leq \sigma_{\text{scatt}} \leq 0.5$ in steps of 0.5. We chose $0.5\sigma_{\text{scatt}}$ as an

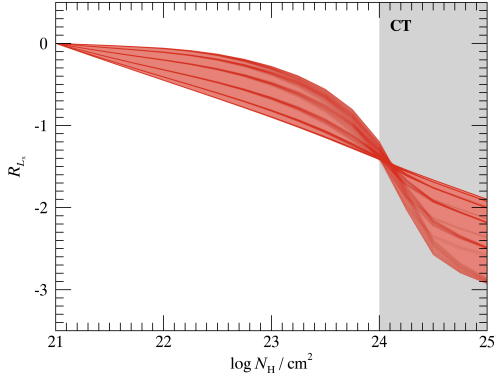


Figure 2. Observed-to-intrinsic X-ray luminosity ratio R_{LX} as a function of obscuring column density N_H . The shaded region of R_{LX} - N_H shown here represents the continuous parameter space inferred from our full suite of X-ray spectral models and parameters $\{f_{\text{scatt}}, R, \Gamma, \theta_{\text{OA}}\}$. Of these parameters we find f_{scatt} to have the most significant effect on R_{LX} , as seen by the striations, or channels, caused by our choice of step size in f_{scatt} parameter space. The remaining parameters R, Γ , and θ_{OA} are responsible for the narrow scatter within each of the deeper channels attributed to f_{scatt} . The vertical shaded gray region demarcates Compton-thick levels of obscuration ($N_H > 10^{24} \text{ cm}^{-2}$).

upper limit as sources with little or no obscuration would produce nonphysical results (i.e., total emission scattered greater than 100%). We allowed the reflection scaling factor to vary between $0.0 \leq R \leq 2.0$ in steps of 0.2, where $R = 0.0$ corresponds to Compton reflection solely from the back-side of the torus (i.e., no disk reflection). We allowed photon index to vary in steps of 0.1 between $1.4 \leq \Gamma \leq 2.2$ to span the full range observed in AGN samples. Finally, we allowed the opening angle to vary in steps of 10° , spanning a range from $10^\circ \leq \theta_{\text{OA}} \leq 80^\circ$.

The relation between R_{LX} and N_H from our models is shown in Figure 2. Of our choice of parameters, variance on f_{scatt} had the most significant effect on R_{LX} , causing large striations, or channels, to develop in R_{LX} - N_H . Aside from f_{scatt} , our other parameters show little to no effect on R_{LX} . Additionally, [Ananna et al. \(2020\)](#) ruled out regions of X-ray spectral parameter space where AGNs could not reliably reproduce the CXB. As these parameters also produce no significant effect on our results, we chose set values moving forward to save computational costs. For the remainder of this work, we adopted R_{LX} values from our X-ray models where $\Gamma = 1.9$, $R = 0.99$, and $\theta_{\text{OA}} = 60^\circ$. A subset of our X-ray spectral models are presented in Figure 3.

We then evaluated the observed-frame output of the model for a range of redshifts to cover our sample redshift space ($0.0 \leq z \leq 0.8$). At each redshift, we calculated X-ray spectral model fluxes in the observed 0.5–2 and 2–7 keV bands. A comparison between the observed soft and hard fluxes with rest-frame 2–10 keV flux provides us with a way to estimate

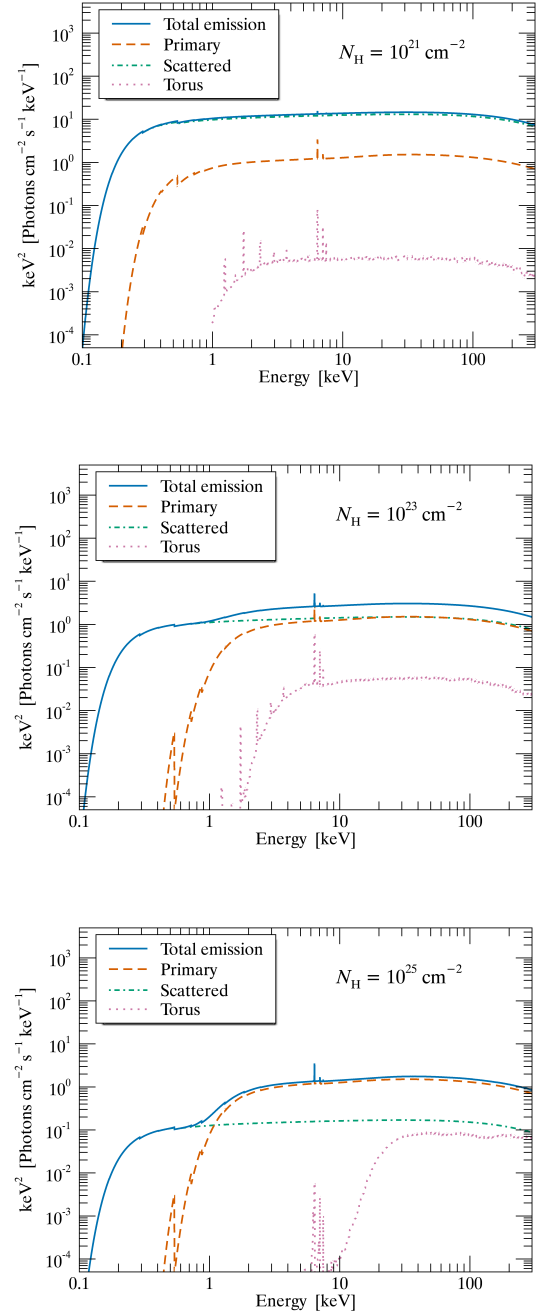


Figure 3. X-ray spectral energy distributions. Variation in the observed-frame X-ray spectra is shown with changes to the absorbing column density N_H . To assist with visualization, we show three cases: $N_H = 10^{21} \text{ cm}^{-2}$ (top); $N_H = 10^{23} \text{ cm}^{-2}$ (middle); and $N_H = 10^{25} \text{ cm}^{-2}$ (bottom). The total X-ray SED is shown (solid blue) as well as the individual components: primary power-law continuum disk emission (dashed orange), scattered primary emission (dash-dotted green), and reprocessed torus emission (dotted magenta).

0.5–2 and 2–7 keV fluxes we would expect to observe for a given model distribution of N_{H} .

3.2. Modeling the Compton-thick Fraction

We used the Bayesian ensemble sampler `emcee` (Foreman-Mackey et al. 2013) to forward model the observed R_{L_X} distribution of our sample and estimate the total fraction of CT AGNs. Using the connection between AGN X-ray flux and nuclear obscuration explored in Section 3.1, we created model N_{H} distributions which we then converted to distributions in R_{L_X} . We then used these model distributions $M(R_{L_X})$ to infer the likelihood of observing our sample data.

At each step of the MCMC, we used the model parameter f_{CT} to create a random sample in N_{H} covering a range of column densities (see Figure 4). For column densities up to 10^{24} cm^{-2} , we assumed the intrinsic column density distribution of Ricci et al. (2017) for non-blazar AGNs. As C21 focused primarily on the detection of heavily obscured sources, their final sample lacks a significant fraction of true unobscured, Type-I AGNs ($N_{\text{H}} \approx 10^{20} \text{ cm}^{-2}$). Considering the lack of dynamic range in R_{L_X} where $N_{\text{H}} < 10^{21} \text{ cm}^{-2}$, we chose to modify the input N_{H} distribution by removing all sources with column densities $N_{\text{H}} < 10^{21} \text{ cm}^{-2}$. We further tested our modeling with a different input N_{H} distributions (i.e., the NuSTAR informed distribution of Lansbury et al. 2015) and found no significant change in our results, indicating that uncertainties on the fraction of fully unobscured sources does not play a significant role in our modeling and results. We made limited assumptions regarding the number of sources and shape of the underlying distribution for $N_{\text{H}} \geq 10^{24} \text{ cm}^{-2}$. Specifically, we set the upper limit of our model to $N_{\text{H}} = 10^{26} \text{ cm}^{-2}$, as densities approaching this limit have only recently been detected (e.g., Yan et al. 2019). The fraction of heavily obscured sources was allowed to vary between $0.00 < f_{\text{CT}} < 1.00$, and the Compton scattering fraction f_{scatt} was allowed to vary within the G21 uncertainties. A flat prior was assumed on both parameters.

Although f_{CT} and f_{scatt} are the only free parameters in our simulation, we also considered the shape of the N_{H} distribution for sources with high obscuration ($N_{\text{H}} \geq 10^{24} \text{ cm}^{-2}$). We allowed the fraction of sources with column densities $10^{24}–10^{25} \text{ cm}^{-2}$ and $10^{25}–10^{26} \text{ cm}^{-2}$ (f_{24-25} and f_{25-26} , respectively) to vary, where the combined fractions account for the full number of CT sources in any given model. We performed multiple runs of our simulation to assess the influence a higher fraction of extremely obscured sources ($f_{24-25} < f_{25-26}$) would have on our parameter estimates. As shown in Figure A1, we find that varying f_{24-25} shows a negligible effect on f_{CT} , but shares a positive correlation with f_{scatt} . As the number of heavily obscured sources rises (i.e., f_{25-26} increases), a slight increase in f_{scatt} is required to model the data (i.e., the uncertainty on scatter fraction σ_{scatt} moves closer to zero). Variations on f_{24-25} and f_{25-26} produce trivial change in our parameter estimation, therefore we adopt a uniform N_{H} distribution where $f_{24-25} = f_{25-26}$ for our simulation. Additionally, we ran similar tests for a range of

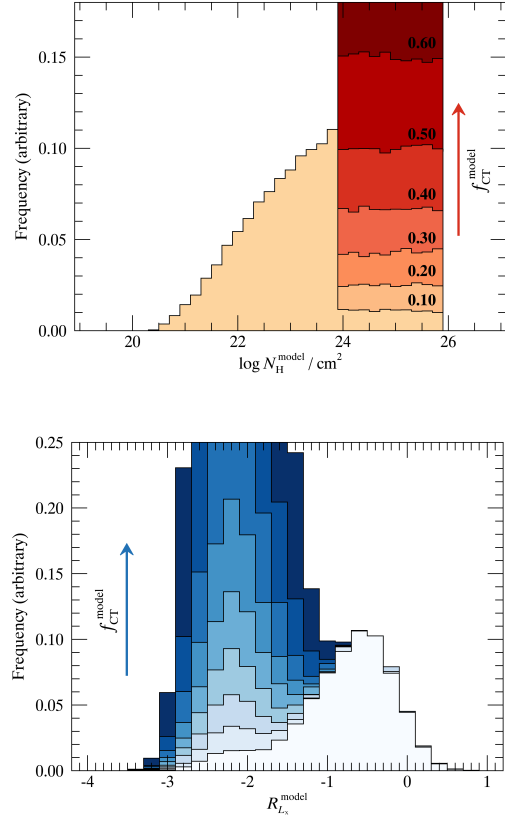


Figure 4. Upper panel: Example N_{H} model distributions from our simulation, where each model is generated with varying f_{CT} . This figure represents a small subset of possible N_{H} distributions, presented here in steps of $\Delta f_{\text{CT}} = 0.10$ with uniformly distributed number of sources at $N_{\text{H}} > 10^{24} \text{ cm}^{-2}$ for clarity. Lower panel: Corresponding R_{L_X} distributions.

parameters $\{R, \Gamma, \theta_{\text{OA}}\}$, the results of which are shown in Figures A2 and A3.

Our simulation aimed to estimate f_{CT} from a sample of 540 IR-luminous AGNs, many of which lack X-ray counterparts. To accomplish this, we modeled both the intrinsic number of sources expected in the survey as well as the expected observed sample size, based on both our model and X-ray flux sensitivity limits. We assumed a log-likelihood function of the form

$$\ln \mathcal{L} = \sum_{i=1}^{N_{\text{det}}} \ln \int M(R_{L_X}) \mathcal{N}(R_{L_X, i}, 0.23) dR_{L_X} - \int M(R_{L_X}) \sum_{i=1}^{N_{\text{all}}} S_i(R_{L_X, \text{lim}}) dR_{L_X} \quad (2)$$

to account for both X-ray detected and non-detected sources. A detailed description of the two terms in our likelihood function follows. A visual representation of $M(R_{L_X})$ and

both terms of our likelihood are presented in Figures B1, B2, and B3, respectively.

The first term of Equation 2 sums over all model distributions for the X-ray detected sources in our sample. Here, $M(R_{L_X})$ represents the normalized model distribution generated at each step in the simulation given a choice of parameters $\{f_{\text{CT}}, f_{\text{scatt}}\}$. For each X-ray detected source, we create a Gaussian distribution $\mathcal{N}(R_{L_X, i}, 0.23)$ centered on the observed R_{L_X} of the source and an uncertainty of 0.23 dex—the intrinsic dispersion in the L_X – L_{MIR} relation. The convolution of these two terms generates a probability density of observing a source given the current choice of parameters at each step in the simulation. We then integrated over all possible R_{L_X} and summed over all of the detected sources in the sample.

The second term of Equation 2 acts as a normalizing constant and accounts for all sources in the sample. Again, $M(R_{L_X})$ represents the current model at each step in the simulation, but this time before integrating it is multiplied by the sensitivity function $S_i(R_{L_X, \text{lim}})$. To account for observational bias in a flux-limited survey, a complicated calculation of sample incompleteness is generally required. However, we use the fact that R_{L_X} is the logarithmic ratio of X-ray luminosities to our advantage, and instead calculated $R_{L_X, \text{lim}}$ using the X-ray flux-limit luminosity of each source (see Equation 1). Using $R_{L_X, \text{lim}}$ in this way allows us to estimate whether an object would be detected at any given step in our simulation. As such, the sensitivity function $S_i(R_{L_X, \text{lim}})$ is a Heaviside function, shifted by $R_{L_X, \text{lim}}$, or

$$S_i(R_{L_X, \text{lim}}) = \Theta(R_{L_X} - R_{L_X, \text{lim}, i}). \quad (3)$$

As before, we convolved $M(R_{L_X})$ with $S_i(R_{L_X, \text{lim}})$ and integrated over the full sample. The second term of Equation 2 therefore serves as the expected observed sample size, penalizing our likelihood function where $M(R_{L_X})$ does not produce a comparable number of detected sources.

The ensemble sampler was run with 80 walkers, each with 1000 steps and a burn-in period of 50 steps. Convergence of the walkers was assessed within `emcee` using the Gelman-Rubin statistic. The posterior distributions of our parameters were estimated by combining the results of all walkers using the ensemble average (see Figure 5).

4. RESULTS AND CONCLUSIONS

The posterior mean f_{CT} is estimated to be $0.555^{+0.037}_{-0.032}$, which suggests that at least half of all MIR-selected AGNs out to $z \leq 0.8$ are heavily obscured, with hydrogen column densities on the order of $\sim 10^{24} \text{ cm}^{-2}$ or higher. Uncertainties on f_{CT} were inferred from our modeling procedure, which accounted for a variety of parameters (e.g., scattering fraction) and assumptions (e.g., choice of input N_{H} distribution). Our results are in remarkable agreement with A19 that estimates a luminosity dependent CT fraction on the order of 0.50–0.56 at comparable redshifts ($z \leq 1$ compared to $z \leq 0.8$ in this work). Most notable is our arrival at nearly identical results using completely independent methods—we make

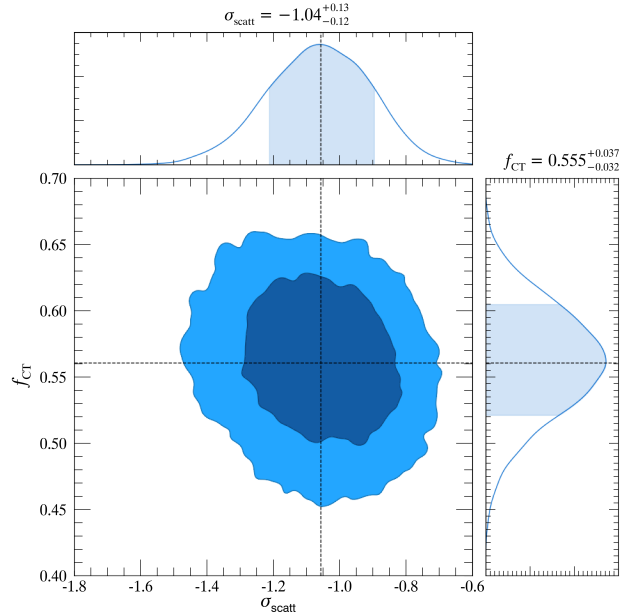


Figure 5. Posterior distributions of our modeling parameters, f_{CT} and σ_{scatt} . The mean and covariance of each parameter is shown alongside its respective distribution.

no use of AGN XLF, nor adjust our methodology to account for the integrated CXB.

We further used our results to infer the distribution of AGN obscuration, including contribution from unidentified CT AGNs. To derive a comprehensive estimate, we used the intrinsic N_{H} distribution of Ricci et al. (2017)—complete with unobscured sources (i.e., $N_{\text{H}} < 10^{21} \text{ cm}^{-2}$)—as our input distribution. We generated 10,000 N_{H} distributions following the prescription detailed in Section 3, but instead fix the CT fraction to $f_{\text{CT}} = 0.555^{+0.037}_{-0.032}$. We then converted N_{H} to $M(R_{L_X})$ assuming a Gaussian distribution $\mathcal{N}(-1, 0.8)$ for the uncertainties on f_{scatt} and the same choice of spectral parameters described in Section 3.1. Each simulated source was then randomly assigned to an object in our sample. We compared $M(R_{L_X})$ to $R_{L_X, \text{lim}}$ and flagged each simulated source as “detected” where $M(R_{L_X}) \geq R_{L_X, \text{lim}}$ and “non-detected” where $M(R_{L_X}) < R_{L_X, \text{lim}}$. Finally, we averaged and normalized ($N_{\text{H}} < 10^{24} \text{ cm}^{-2}$) over all N_{H} distributions. Our results modeling the N_{H} distribution of MIR-selected AGNs is presented in the lower panel of Figure 6.

We then compared our inferred N_{H} distribution to that of A19. As their results are luminosity dependent, we averaged over both A19 N_{H} distributions, weighted by the fraction of our sample sources in each respective luminosity bin (0.21 and 0.79; split on $\log L_X/\text{erg s}^{-1} = 43.6$). Comparing these results in Figure 6, we find a striking similarity between our work and that of A19. Though previous estimates of the CT fraction using the AGN XLF have sometimes yielded drastically different results, our determination of the CT fraction and estimated N_{H} distribution is in close agreement with

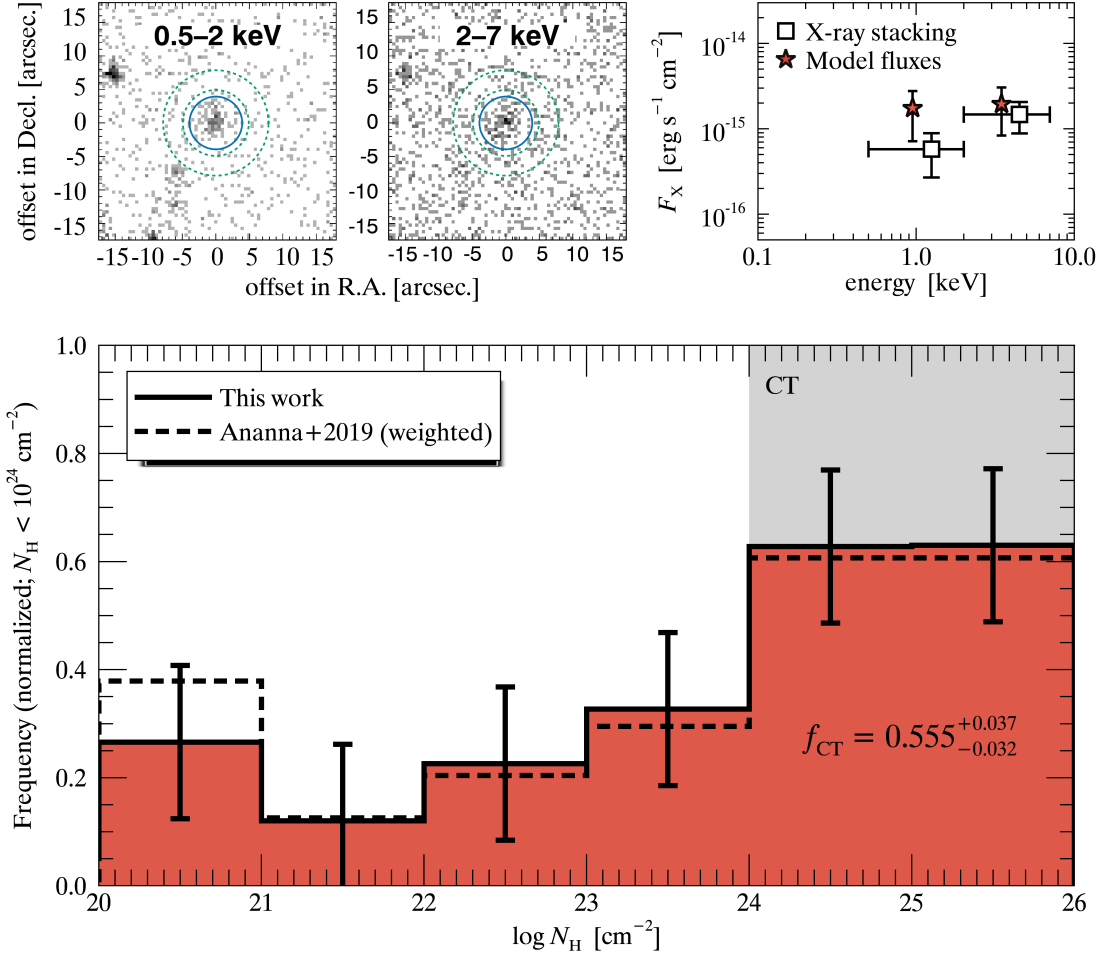


Figure 6. Modeling results. Top left: Soft (0.5–2 keV) and hard (2–7 keV) band stacked images for the X-ray non-detected sources in our sample using STACKFAST (Ananna 2023, in prep.). Source extraction regions are represented by the solid blue circles, while background subtraction regions are depicted by the dashed green annuli. Top right: Comparison of the X-ray stacked fluxes (squares) to estimates on observed fluxes from our modeling (stars). Model fluxes were plotted with horizontal offsets for visual clarity. Bottom panel: N_H distribution with predicted CT fraction of $0.555^{+0.037}_{-0.032}$ from our simulation (solid line). The estimated N_H distribution of A19 is shown for reference (dashed line), where the synthesis model estimates are represented as a weighted average of our sample sources with low ($\log L_X(L_{\text{MIR}})/\text{erg s}^{-1} < 43.6$) and high ($\log L_X(L_{\text{MIR}})/\text{erg s}^{-1} \geq 43.6$) intrinsic X-ray luminosity. The vertical shaded gray region demarcates Compton-thick levels of obscuration ($N_H > 10^{24}$ cm $^{-2}$). Sources with $N_H < 10^{20}$ cm $^{-2}$ (due to scatter converting between R_{L_X} and N_H) were reassigned to $N_H = 10^{20}$ cm $^{-2}$ for clarity.

Finally, we considered whether f_{CT} and the N_H distribution predicted by our modeling would produce similar soft and hard X-ray fluxes comparable to measurements obtained from X-ray stacking. We performed an X-ray stacking analysis of sources in Chandra fields using STACKFAST (Ananna 2023, in prep.). To ensure accuracy, we restricted our comparison to sources in fields observed by Chandra, rather than XMM or NuSTAR, as the high angular resolution of Chandra allows for more robust X-ray stacking measurements. Of the

A19, using completely different measurement techniques and methodologies.

540 sources in our dataset, 151 sources lie within observed Chandra fields (60 X-ray detected; 91 X-ray non-detected). For each of our X-ray non-detected sources we extracted photon counts and exposure times in both soft (0.5–2 keV) and hard (2–7 keV) energies. We computed fluxes using count-rate-to-flux ratios characteristic of our X-ray spectral models (see Section 3.1), and assumed a power law spectrum with photon index $\Gamma = 1.8$ and typical Galactic absorption ($N_H = 10^{20}$ cm $^{-2}$) as is typical of observed AGN X-ray spectra. We adopted count-rate-to-flux conversion factor of 3.61×10^{-12} erg cm $^{-2}$ count $^{-1}$ and 7.44×10^{-12} erg cm $^{-2}$

Table 1. X-ray stacking results and model comparison.

	t_{exp}	Energy	N_{src}	N_{bkg}	N_{net}	$F_{\text{X}}^{\text{stack}}$	$F_{\text{X}}^{\text{model}}$
	[Ms]	[keV]				[$\text{erg s}^{-1} \text{cm}^{-2}$]	[$\text{erg s}^{-1} \text{cm}^{-2}$]
WISE AGN (X-ray non-det.)	1.49	0.5–2	740	634	106	$5.78 \pm 3.09 \times 10^{-16}$	$1.74 \pm 1.02 \times 10^{-15}$
		2–7	1328	1219	109	$1.47 \pm 0.59 \times 10^{-15}$	$1.94 \pm 1.11 \times 10^{-15}$

NOTE—X-ray stacking results for energy ranges of 0.5–2 and 2–7 keV with STACKFAST. For each energy range, we present exposure time, photon counts (source, background, and net), and stacked flux estimates. The final column depicts mean estimates of observed fluxes from our modeling.

count⁻¹ for 0.5–2 and 2–7 keV, respectively. Fluxes calculated from our count-rate-to-flux conversion are representative of Chandra ACIS-I Cycle 12 responses—the current cycle for the majority of the observations in our stacking analysis. Uncertainties on the stacked fluxes were estimated by bootstrap resampling of input sources. The calculated uncertainties therefore reflect the distribution of input fluxes and are generally larger than Poisson uncertainties. Although our choice of X-ray spectral models in Section 3.1 includes additional components, the spectral shape chosen for our count-rate-to-flux conversion is consistent in the energy range considered in this work (2–10 keV) and was deemed sufficient for our analysis.

To estimate the observed X-ray fluxes from our model, we randomly assigned each simulated sources previously flagged as non-detected to one of the 91 X-ray non-detected Chandra sources in our sample. We extracted rest-frame 2–10 keV luminosities for each model source using the combination of $R_{L_X}^{\text{model}}$ and $L_X(L_{\text{MIR}})$. We then converted the rest-frame 2–10 keV luminosities to observed 0.5–2 and 2–7 keV fluxes using the X-ray spectral conversions discussed in Section 3.1. To account for possible contamination in the data, we randomly set the X-ray flux for 10% of all model sources to zero. We chose to remove 10% of model sources to match the WISE AGN R90 catalog (Assef et al. 2018), which assesses 90% reliability in their AGN selection methods. Though recent work has suggested that the level of contamination may be higher (e.g., Hainline et al. 2016; LaMassa et al. 2019), we found that varying the fraction of contamination between 5%–20% had a negligible effect on our results. We repeated this process 100 times and calculated the mean flux over all model sources.

The results of both our X-ray stacking and model estimates are presented in Table 1, while a side-by-side visual comparison is also shown in the top panel of Figure 6. We find our model fluxes to be in good agreement with the X-ray stacking results to within 0.48 dex at soft energies (0.5–2 keV) and 0.12 dex at hard energies (2–7 keV). While our hard X-ray fluxes are in excellent agreement with our stacking results, our soft X-ray fluxes estimates are three times higher than our stacking results. An increase in X-ray photons at soft energies could possibly be due to overestimation of the reflection strength parameter R used in our spectral models.

In fact, one postulated explanation of the soft X-ray excess found in nearly half of all nearby AGNs is upscattered X-ray photons reflecting back off of the accretion disk. Though this model may be losing favor (e.g., Done & Nayakshin 2007; Ursini et al. 2020), it stands that reflection does contribute to an increase in soft X-rays. The discrepancy between the soft X-ray fluxes of our model and stacking may be caused by a relatively high amount of Compton scattering, generally attributed to Type-I AGNs.

We also considered whether the X-ray selection of targeted sources may bias our results. To test this we removed targets close to field centers (at both 0.5' and 1') and reran our analysis to track any changes. In the end, we found no appreciable differences in our results. We find that the fraction of detected sources actually increases linearly with distance from field center. Because of this, we do not believe there is any significant bias introduced by combining X-ray targeted sources with serendipitous sources. It is possible that detection of point sources in the vicinity of targeted bright X-ray objects could be limited by diffuse emission, but this is not something we can currently account for.

5. DISCUSSION

Our approach differs from previous work in distinct ways: modeling of the observed R_{L_X} distribution (i.e., a measurable proxy for nuclear obscuration) in lieu of assumptions on N_{H} distribution; the choice of generalized X-ray spectral models, accounting for fewer parameters, degrees of freedom, and potential degeneracies; constraints from X-ray stacking of individual sources rather than an integrated spectrum, such as the CXB. Whereas synthesis models may fit obscured and unobscured AGNs separately to estimate the overall XLF, our technique relies solely on direct observables (i.e., X-ray and infrared observations) to infer the overall distribution of CT AGNs from simulated N_{H} distributions. Our approach of forward modeling the observed R_{L_X} distribution allows us to deduce the fraction of CT AGNs without assumptions and uncertain completeness corrections on the number of sources or the shape of the N_{H} distribution for heavily obscured sources.

There are a number of broad implications for a high fraction of CT AGNs, but one direct consequence involves BH accretion physics. A significant increase in the number of heavily obscured AGNs, missing in typical X-ray observa-

tions, may signify an increase in the average cosmic accretion efficiency driving BH growth (i.e., [Comastri et al. 2015](#)). The BH mass function, which provides a record of the mass of SMBHs in the local universe, in turn provides information on the accretion history of SMBHs. An increase in the integrated energy density due to AGNs would necessitate an increase in the efficiency of accretion, under the assumption that the empirically derived BH mass function is a statistically complete relation (i.e., [Blecha et al. 2016](#)). As the AGN community converges on the true underlying population of actively accreting SMBHs in the Universe, we can take further steps to painting a more complete picture of galaxy and AGN co-evolution and the role AGNs play in other observables, such as the CXB.

Furthermore, significant efforts have been made to understand the importance of major mergers on the activity and duty cycle of AGNs. Though the significance of mergers as a primary driver of SMBH growth remains a matter of active investigation, clear evidence is seen for an increase in the fraction of disturbed host morphologies in heavily obscured and CT AGNs (e.g., [Kocevski et al. 2015](#)). While mergers are predicted to provide gas which may obscure AGNs at host galaxy scales (e.g., [Blecha et al. 2018](#)), the results presented in this work deal primarily with nuclear attenuation. A follow-up study on the host morphologies of our sample, which include many CT AGNs yet undetected at X-ray energies, could provide valuable insight on potential biases due to AGN selection methods in such studies. If the “missing” CT AGNs in our sample are found to have particular galaxy morphologies, this would provide further evidence for a scenario in which CT AGN can be obscured by material on scales beyond the central torus and may represent a distinct phase of SMBH growth ([Sanders et al. 1988](#)).

Future work may attempt to extrapolate our estimate of the Compton-thick fraction from a MIR-selected sample to the full AGN population. A full accounting of observational biases must be considered to ensure a complete working sample of AGNs collected from different selection techniques at various wavelengths.

1 We thank the referee for exceptionally thoughtful and constructive comments which led to a substantial improvement
2 of this work.
3

4 This research has made use of X-ray data from the following: the NuSTAR mission, a project led by the California Institute of Technology, managed by the Jet Propulsion Laboratory, and funded by the National Aeronautics and Space Administration (NASA); the Chandra Source Catalog 2.0, provided by the Chandra X-ray Center (CXC) as part of the Chandra Data Archive; XMM-Newton, a European Space Agency (ESA) science mission with instruments and contributions directly funded by ESA Member States and NASA.
5
6
7
8
9
10
11
12
13 This research also made use of data products from the Wide-field Infrared Survey Explorer, which is a joint project of the University of California, Los Angeles, and the Jet Propulsion Laboratory/California Institute of Technology, and funded by NASA. This work is also based in part on NIR data obtained as part of the UKIRT Infrared Deep Sky Survey, as well as data products from the Two Micron All Sky Survey, which is a joint project of the University of Massachusetts and the Infrared Processing and Analysis Center/California Institute of Technology, funded by NASA and the National Science Foundation.
14
15
16
17
18
19
20
21
22
23

24 This research also made use of software provided by the High Energy Astrophysics Science Archive Research Center (HEASARC), which is a service of the Astrophysics Science Division at NASA/GSFC and the High Energy Astrophysics Division of the Smithsonian Astrophysical Observatory.
25
26
27
28

29 C.M.C. acknowledges support from the John Templeton Foundation through LSSTC Catalyst Fellowship grant number 62192. C.J.C., R.C.H., and T.T.A. acknowledge support from the NSF through CAREER award number 1554584.
30
31
32
33 R.C.H. and T.T.A. acknowledge support from NASA through ADAP grant number 80NSSC19K0580. T.T.A. also acknowledges support from NASA ADAP grant number 80NSSC23K0557. R.J.A. was supported by FONDECYT grant number 1191124 and 1231718, and by ANID BASAL project FB210003.
34
35
36
37
38

Facilities: Chandra, GALEX, MMT, NuSTAR, SDSS, UKIRT, WISE, XMM, 2MASS

Software: `emcee`: The MCMC Hammer ([Foreman-Mackey et al. 2013](#)), `XSPEC` ([Arnaud 1996](#))

APPENDIX

A. ADDITIONAL PARAMETER TESTS

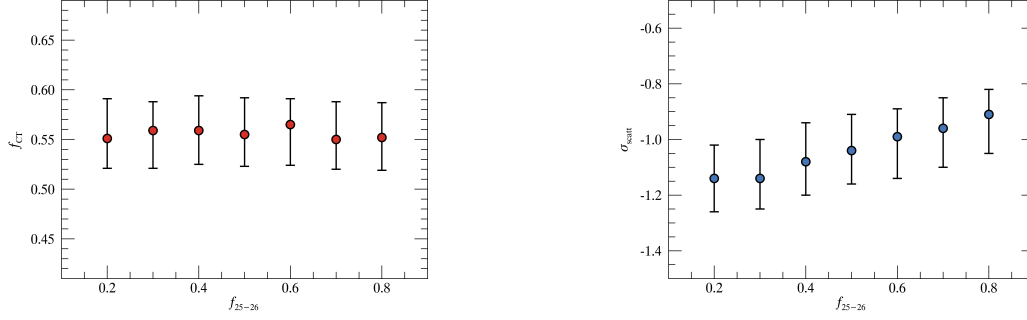


Figure A1. Effects on parameter estimates for a variable distribution of CT sources. Left: Estimates on f_{CT} for increasing fraction of heavily obscured sources f_{25-26} . Right: Similar estimates on σ_{scatt} .

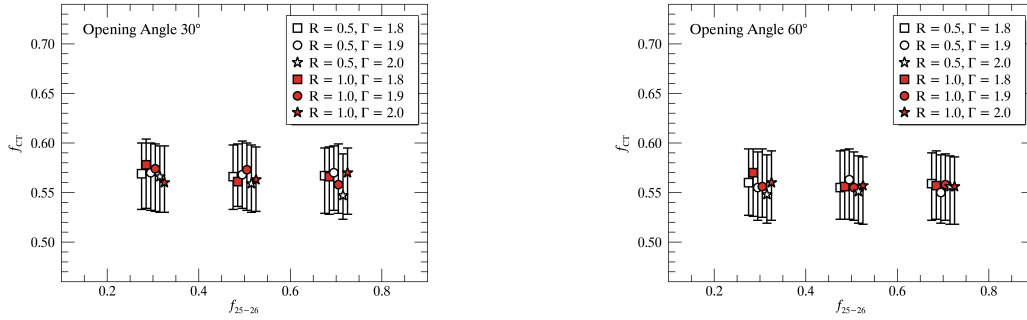


Figure A2. Additional parameter tests— f_{CT} . Left: Compton-thick fraction f_{CT} as a function of f_{25-26} $\{0.3, 0.5, 0.7\}$ for an opening angle of $\theta_{OA} = 30^\circ$. Variations on reflection strength R $\{0.5, 1.0\}$ (open and closed symbols) and photon index Γ $\{1.8, 1.9, 2.0\}$ (squares, circles, and stars) show negligible impact on f_{CT} . Symbols are plotted with horizontal offset for visual clarity. Right: Similar plot, but for an opening angle of $\theta_{OA} = 60^\circ$.

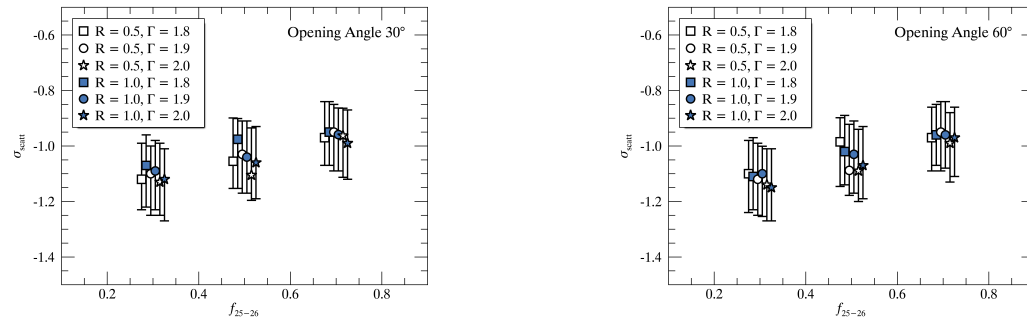


Figure A3. Additional parameter tests— f_{scatt} . Left: Uncertainties on scattering fraction σ_{scatt} as a function of f_{25-26} $\{0.3, 0.5, 0.7\}$ for an opening angle of $\theta_{OA} = 30^\circ$. Variations on reflection strength R $\{0.5, 1.0\}$ (open and closed symbols) and photon index Γ $\{1.8, 1.9, 2.0\}$ (squares, circles, and stars) show negligible impact on σ_{scatt} . Symbols are plotted with horizontal offsets for visual clarity. Right: Similar plot, but for an opening angle of $\theta_{OA} = 60^\circ$.

B. LOG-LIKELIHOOD FUNCTION

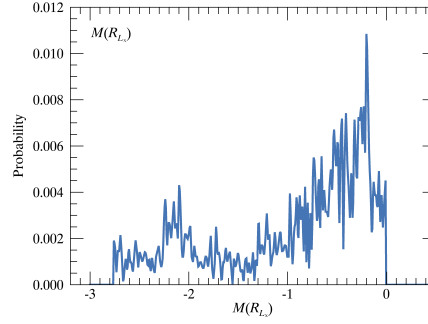


Figure B1. Example $M(R_{L_X})$ given a set of parameters $\{f_{\text{CT}}, f_{\text{scat}}\}$.

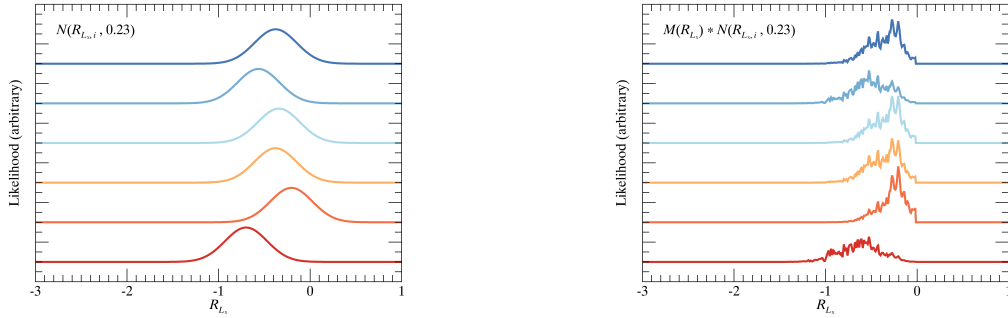


Figure B2. Integrand of the likelihood function—first term. Left: Observed $(R_{L_X,i}, 0.23)$ distribution. Right: Observed $(R_{L_X,i}, 0.23)$ distribution convolved with the model $M(R_{L_X})$. Note that each curve represents an X-ray detected source from our sample. The first term of the likelihood function (Equation 2) is the sum of the logarithm of the integral of these functions.

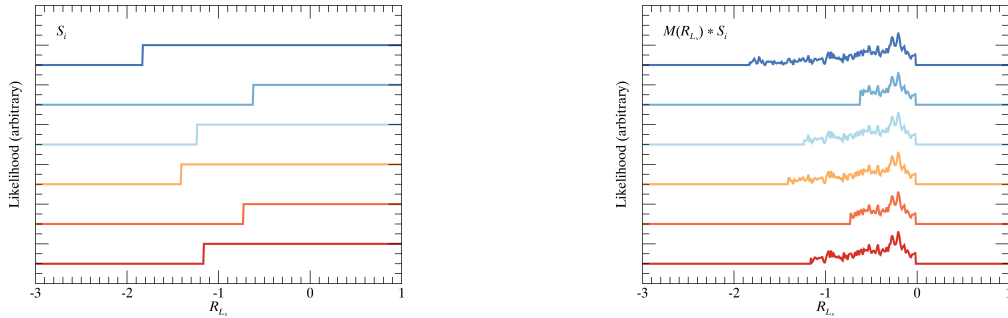


Figure B3. Integrand of the likelihood function—second term. Left: Sensitivity function $S_i(R_{L_X,\text{lim}})$. Right: Sensitivity function $S_i(R_{L_X,\text{lim}})$ convolved with the model $M(R_{L_X})$. Note that each curve represents a different object in the sample (both X-ray detected and non-detected). The second term of the likelihood function (Equation 2) is the sum of these functions, integrated over R_{L_X} .

REFERENCES

- Abolfathi, B., Aguado, D. S., Aguilar, G., et al. 2018, *ApJS*, 235, 42, doi: [10.3847/1538-4365/aa9e8a](https://doi.org/10.3847/1538-4365/aa9e8a)
- Aird, J., Coil, A. L., Georgakakis, A., et al. 2015, *MNRAS*, 451, 1892, doi: [10.1093/mnras/stv1062](https://doi.org/10.1093/mnras/stv1062)
- Ananna, T. T. 2023, in prep., *ApJ*
- Ananna, T. T., Treister, E., Urry, C. M., et al. 2020, *ApJ*, 889, 17, doi: [10.3847/1538-4357/ab5aef](https://doi.org/10.3847/1538-4357/ab5aef)
- . 2019, *ApJ*, 871, 240, doi: [10.3847/1538-4357/aafb77](https://doi.org/10.3847/1538-4357/aafb77)
- Ananna, T. T., Weigel, A. K., Trakhtenbrot, B., et al. 2022a, *ApJS*, 261, 9, doi: [10.3847/1538-4365/ac5b64](https://doi.org/10.3847/1538-4365/ac5b64)
- Ananna, T. T., Urry, C. M., Ricci, C., et al. 2022b, *ApJL*, 939, L13, doi: [10.3847/2041-8213/ac9979](https://doi.org/10.3847/2041-8213/ac9979)
- Antonucci, R. R. J., & Miller, J. S. 1985, *ApJ*, 297, 621, doi: [10.1086/163559](https://doi.org/10.1086/163559)
- Arnaud, K. A. 1996, in *Astronomical Society of the Pacific Conference Series*, Vol. 101, *Astronomical Data Analysis Software and Systems V*, ed. G. H. Jacoby & J. Barnes, 17
- Assef, R. J., Stern, D., Noirot, G., et al. 2018, *ApJS*, 234, 23, doi: [10.3847/1538-4365/aaa00a](https://doi.org/10.3847/1538-4365/aaa00a)
- Assef, R. J., Kochanek, C. S., Brodwin, M., et al. 2010, *ApJ*, 713, 970, doi: [10.1088/0004-637X/713/2/970](https://doi.org/10.1088/0004-637X/713/2/970)
- Assef, R. J., Eisenhardt, P. R. M., Stern, D., et al. 2015, *ApJ*, 804, 27, doi: [10.1088/0004-637X/804/1/27](https://doi.org/10.1088/0004-637X/804/1/27)
- Baloković, M., Brightman, M., Harrison, F. A., et al. 2018, *ApJ*, 854, 42, doi: [10.3847/1538-4357/aaa7eb](https://doi.org/10.3847/1538-4357/aaa7eb)
- Blecha, L., Snyder, G. F., Satyapal, S., & Ellison, S. L. 2018, *MNRAS*, 478, 3056, doi: [10.1093/mnras/sty1274](https://doi.org/10.1093/mnras/sty1274)
- Blecha, L., Sijacki, D., Kelley, L. Z., et al. 2016, *MNRAS*, 456, 961, doi: [10.1093/mnras/stv2646](https://doi.org/10.1093/mnras/stv2646)
- Buchner, J., Georgakakis, A., Nandra, K., et al. 2014, *A&A*, 564, A125, doi: [10.1051/0004-6361/20132297110.48550/arXiv.1402.0004](https://doi.org/10.1051/0004-6361/20132297110.48550/arXiv.1402.0004)
- . 2015, *ApJ*, 802, 89, doi: [10.1088/0004-637X/802/2/89](https://doi.org/10.1088/0004-637X/802/2/89)
- Carroll, C. M., Hickox, R. C., Masini, A., et al. 2021, *ApJ*, 908, 185, doi: [10.3847/1538-4357/abd185](https://doi.org/10.3847/1538-4357/abd185)
- Chen, C.-T. J., Hickox, R. C., Alberts, S., et al. 2015, *ApJ*, 802, 50, doi: [10.1088/0004-637X/802/1/50](https://doi.org/10.1088/0004-637X/802/1/50)
- Chen, C.-T. J., Hickox, R. C., Goulding, A. D., et al. 2017, *ApJ*, 837, 145, doi: [10.3847/1538-4357/837/2/145](https://doi.org/10.3847/1538-4357/837/2/145)
- Civano, F., Hickox, R. C., Puccetti, S., et al. 2015, *ApJ*, 808, 185, doi: [10.1088/0004-637X/808/2/185](https://doi.org/10.1088/0004-637X/808/2/185)
- Comastri, A., Gilli, R., Marconi, A., Risaliti, G., & Salvati, M. 2015, *A&A*, 574, L10, doi: [10.1051/0004-6361/201425496](https://doi.org/10.1051/0004-6361/201425496)
- Davies, R. I., Burtcher, L., Rosario, D., et al. 2015, *ApJ*, 806, 127, doi: [10.1088/0004-637X/806/1/127](https://doi.org/10.1088/0004-637X/806/1/127)
- DiPompeo, M. A., Myers, A. D., Hickox, R. C., Geach, J. E., & Hainline, K. N. 2014, *MNRAS*, 442, 3443, doi: [10.1093/mnras/stu1115](https://doi.org/10.1093/mnras/stu1115)
- DiPompeo, M. A., Myers, A. D., Hickox, R. C., et al. 2015, *MNRAS*, 446, 3492, doi: [10.1093/mnras/stu2341](https://doi.org/10.1093/mnras/stu2341)
- Done, C., & Nayakshin, S. 2007, *MNRAS*, 377, L59, doi: [10.1111/j.1745-3933.2007.00303.x](https://doi.org/10.1111/j.1745-3933.2007.00303.x)
- Evans, I. N., Primini, F. A., Miller, J. B., et al. 2020, in *American Astronomical Society Meeting Abstracts*, Vol. 235, *American Astronomical Society Meeting Abstracts #235*, 154.05
- Fiore, F., Puccetti, S., Brusa, M., et al. 2009, *ApJ*, 693, 447, doi: [10.1088/0004-637X/693/1/447](https://doi.org/10.1088/0004-637X/693/1/447)
- Foreman-Mackey, D., Hogg, D. W., Lang, D., & Goodman, J. 2013, *PASP*, 125, 306, doi: [10.1086/670067](https://doi.org/10.1086/670067)
- Fotopoulou, S., Buchner, J., Georgantopoulos, I., et al. 2016, *A&A*, 587, A142, doi: [10.1051/0004-6361/201424763](https://doi.org/10.1051/0004-6361/201424763)
- García-Burillo, S., Combes, F., Ramos Almeida, C., et al. 2016, *ApJL*, 823, L12, doi: [10.3847/2041-8205/823/1/L12](https://doi.org/10.3847/2041-8205/823/1/L12)
- Gupta, K. K., Ricci, C., Tortosa, A., et al. 2021, *MNRAS*, 504, 428, doi: [10.1093/mnras/stab839](https://doi.org/10.1093/mnras/stab839)
- Hainline, K. N., Reines, A. E., Greene, J. E., & Stern, D. 2016, *ApJ*, 832, 119, doi: [10.3847/0004-637X/832/2/119](https://doi.org/10.3847/0004-637X/832/2/119)
- Hickox, R. C., & Alexander, D. M. 2018, *ARA&A*, 56, 625, doi: [10.1146/annurev-astro-081817-051803](https://doi.org/10.1146/annurev-astro-081817-051803)
- Hickox, R. C., Jones, C., Forman, W. R., et al. 2007, *ApJ*, 671, 1365, doi: [10.1086/523082](https://doi.org/10.1086/523082)
- Hönig, S. F., Kishimoto, M., Antonucci, R., et al. 2012, *ApJ*, 755, 149, doi: [10.1088/0004-637X/755/2/149](https://doi.org/10.1088/0004-637X/755/2/149)
- Kirkpatrick, A., Pope, A., Sajina, A., et al. 2015, *ApJ*, 814, 9, doi: [10.1088/0004-637X/814/1/9](https://doi.org/10.1088/0004-637X/814/1/9)
- Kocevski, D. D., Brightman, M., Nandra, K., et al. 2015, *ApJ*, 814, 104, doi: [10.1088/0004-637X/814/2/104](https://doi.org/10.1088/0004-637X/814/2/104)
- Lacy, M., Ridgway, S. E., Gates, E. L., et al. 2013, *ApJS*, 208, 24, doi: [10.1088/0067-0049/208/2/24](https://doi.org/10.1088/0067-0049/208/2/24)
- LaMassa, S. M., Georgakakis, A., Vivek, M., et al. 2019, *ApJ*, 876, 50, doi: [10.3847/1538-4357/ab108b](https://doi.org/10.3847/1538-4357/ab108b)
- LaMassa, S. M., Civano, F., Brusa, M., et al. 2016, *ApJ*, 818, 88, doi: [10.3847/0004-637X/818/1/88](https://doi.org/10.3847/0004-637X/818/1/88)
- Lambrides, E. L., Chiaberge, M., Heckman, T., et al. 2020, *ApJ*, 897, 160, doi: [10.3847/1538-4357/ab919c](https://doi.org/10.3847/1538-4357/ab919c)
- Lang, D. 2014, *AJ*, 147, 108, doi: [10.1088/0004-6256/147/5/108](https://doi.org/10.1088/0004-6256/147/5/108)
- Lansbury, G. B., Gandhi, P., Alexander, D. M., et al. 2015, *ApJ*, 809, 115, doi: [10.1088/0004-637X/809/2/115](https://doi.org/10.1088/0004-637X/809/2/115)
- Lansbury, G. B., Alexander, D. M., Aird, J., et al. 2017, *ApJ*, 846, 20, doi: [10.3847/1538-4357/aa8176](https://doi.org/10.3847/1538-4357/aa8176)
- Lawrence, A., Warren, S. J., Almaini, O., et al. 2007, *MNRAS*, 379, 1599, doi: [10.1111/j.1365-2966.2007.12040.x](https://doi.org/10.1111/j.1365-2966.2007.12040.x)
- López-Gonzaga, N., Burtcher, L., Tristram, K. R. W., Meisenheimer, K., & Schartmann, M. 2016, *A&A*, 591, A47, doi: [10.1051/0004-6361/201527590](https://doi.org/10.1051/0004-6361/201527590)
- Martin, D. C., Fanson, J., Schiminovich, D., et al. 2005, *ApJL*, 619, L1, doi: [10.1086/426387](https://doi.org/10.1086/426387)

- Masini, A., Civano, F., Comastri, A., et al. 2018, *ApJS*, 235, 17, doi: [10.3847/1538-4365/aaa83d](https://doi.org/10.3847/1538-4365/aaa83d)
- Mateos, S., Alonso-Herrero, A., Carrera, F. J., et al. 2013, *MNRAS*, 434, 941, doi: [10.1093/mnras/stt953](https://doi.org/10.1093/mnras/stt953)
- Noguchi, K., Terashima, Y., Ishino, Y., et al. 2010, *ApJ*, 711, 144, doi: [10.1088/0004-637X/711/1/144](https://doi.org/10.1088/0004-637X/711/1/144)
- Panagiotou, C., & Walter, R. 2019, *A&A*, 626, A40, doi: [10.1051/0004-6361/201935052](https://doi.org/10.1051/0004-6361/201935052)
- Pfeifle, R. W., Ricci, C., Boorman, P. G., et al. 2021, arXiv e-prints, arXiv:2102.04412. <https://arxiv.org/abs/2102.04412>
- Ricci, C., Trakhtenbrot, B., Koss, M. J., et al. 2017, *Nature*, 549, 488, doi: [10.1038/nature23906](https://doi.org/10.1038/nature23906)
- Rosen, S. R., Webb, N. A., Watson, M. G., et al. 2016, *A&A*, 590, A1, doi: [10.1051/0004-6361/201526416](https://doi.org/10.1051/0004-6361/201526416)
- Sanders, D. B., Soifer, B. T., Elias, J. H., et al. 1988, *ApJ*, 325, 74, doi: [10.1086/165983](https://doi.org/10.1086/165983)
- Skrutskie, M. F., Cutri, R. M., Stiening, R., et al. 2006, *AJ*, 131, 1163, doi: [10.1086/498708](https://doi.org/10.1086/498708)
- Spergel, D. N., Bean, R., Doré, O., et al. 2007, *ApJS*, 170, 377, doi: [10.1086/513700](https://doi.org/10.1086/513700)
- Stern, D. 2015, *ApJ*, 807, 129, doi: [10.1088/0004-637X/807/2/129](https://doi.org/10.1088/0004-637X/807/2/129)
- Stern, D., Eisenhardt, P., Gorjian, V., et al. 2005, *ApJ*, 631, 163, doi: [10.1086/432523](https://doi.org/10.1086/432523)
- Stern, D., Assef, R. J., Benford, D. J., et al. 2012, *ApJ*, 753, 30, doi: [10.1088/0004-637X/753/1/30](https://doi.org/10.1088/0004-637X/753/1/30)
- Traina, A., Marchesi, S., Vignali, C., et al. 2021, *ApJ*, 922, 159, doi: [10.3847/1538-4357/ac1fee](https://doi.org/10.3847/1538-4357/ac1fee)
- Tristram, K. R. W., Burtscher, L., Jaffe, W., et al. 2014, *A&A*, 563, A82, doi: [10.1051/0004-6361/201322698](https://doi.org/10.1051/0004-6361/201322698)
- Ueda, Y., Akiyama, M., Hasinger, G., Miyaji, T., & Watson, M. G. 2014, *ApJ*, 786, 104, doi: [10.1088/0004-637X/786/2/104](https://doi.org/10.1088/0004-637X/786/2/104)
- Ursini, F., Petrucci, P. O., Bianchi, S., et al. 2020, *A&A*, 634, A92, doi: [10.1051/0004-6361/201936486](https://doi.org/10.1051/0004-6361/201936486)
- Wright, E. L., Eisenhardt, P. R. M., Mainzer, A. K., et al. 2010, *AJ*, 140, 1868, doi: [10.1088/0004-6256/140/6/1868](https://doi.org/10.1088/0004-6256/140/6/1868)
- Yan, W., Hickox, R. C., Hainline, K. N., et al. 2019, *ApJ*, 870, 33, doi: [10.3847/1538-4357/aaed4](https://doi.org/10.3847/1538-4357/aaed4)
- York, D. G., Adelman, J., Anderson, Jr., J. E., et al. 2000, *AJ*, 120, 1579, doi: [10.1086/301513](https://doi.org/10.1086/301513)